

Cryo-EM reveals an electron transfer path in a Mycobacterial respiratory supercomplex

Authors: Hongri Gong^{1†}, Jun Li^{2,3†}, Ao Xu^{1,4†}, Yanting Tang¹, Wenxin Ji^{4,12}, Ruogu Gao^{4,12}, Shuhui Wang^{2,3}, Lu Yu⁵, Changlin Tian^{5,6}, Jingwen Li⁷, Hsin-Yung Yen⁷, Sin Man Lam⁸, Guanghou Shui⁸, Xiuna Yang^{2,3}, Yuna Sun⁴, Xuemei Li⁴, Minze Jia⁴, Cheng Yang¹, Biao Jiang², Zhiyong Lou⁹, Carol V. Robinson⁷, Luet-Lok Wong¹⁰, Luke W. Guddat¹¹, Fei Sun^{4,12*}, Quan Wang^{4*} & Zihe Rao^{1,2,3,4,9*}

Affiliations:

¹State Key Laboratory of Medicinal Chemical Biology, Nankai University, Tianjin 300353, China.

²Shanghai Institute for Advanced Immunochemical Studies, ShanghaiTech University, Shanghai, 201210, China.

³CAS Center for Excellence in Molecular Cell Science, Shanghai Institute of Biochemistry and Cell Biology, Chinese Academy of Sciences, 320 Yueyang Road, Shanghai 200031, China

⁴National Laboratory of Biomacromolecules, CAS Center for Excellence in Biomacromolecules, Institute of Biophysics, Chinese Academy of Sciences, Beijing 100101, China.

⁵High Magnetic Field Laboratory, Chinese Academy of Sciences, Hefei 230031, China

⁶Hefei National Laboratory of Physical Sciences at Microscale and School of Life Sciences, University of Science and Technology of China, Hefei 230027, China.

⁷Department of Chemistry, University of Oxford, Physical and Theoretical Chemistry Laboratory, South Parks Rd, Oxford, OX1 3QZ, UK.

⁸State Key Laboratory of Molecular Developmental Biology, Institute of Genetics and Developmental Biology, Chinese Academy of Sciences, Beijing 100101, China.

⁹Laboratory of Structural Biology, Tsinghua University, Beijing 100084, China.

¹⁰Department of Chemistry, University of Oxford, Inorganic Chemistry Laboratory, South Parks Road, Oxford OX1 3QR, UK.

¹¹School of Chemistry and Molecular Biosciences, The University of Queensland, Brisbane, 4072 Queensland, Australia.

¹²University of Chinese Academy of Sciences, Beijing, China.

*Correspondence authors: ZR (raozh@tsinghua.edu.cn), QW (wangq@ibp.ac.cn) or FS (feisun@ibp.ac.cn).

† These authors contributed equally to the study.

Abstract: We report a 3.5-Å resolution cryo-EM structure of a respiratory supercomplex isolated from *Mycobacterium smegmatis*. It comprises a complex III dimer flanked on either side by individual complex IV subunits. Complex III and IV associate such that electrons can be transferred from quinol in complex III to the oxygen reduction center in complex IV via a bridging cytochrome subunit. We observe a superoxide dismutase-like subunit at the periplasmic face, which may be responsible for detoxification of superoxide formed by complex III. The structure

reveals features of an established drug target and provides a foundation for development of treatments for human tuberculosis.

One Sentence Summary:

The mycobacterial enzyme does not require soluble electron carriers and can associate with superoxide dismutase.

Main Text:

In cellular respiration, chemical energy is extracted by coupling the oxidation of an energy source (e.g. sugars, fatty acids, amino acids) and the reduction of an electron acceptor (e.g. oxygen, sulfur, nitrate, sulfate) to synthesize adenosine triphosphate (ATP) which powers cellular reactions. In aerobic organisms, electrons are transferred from electron donors to oxygen, the terminal acceptor, through the electron transport chain (ETC) to pump protons across a membrane (cellular or mitochondrial). This creates a transmembrane proton gradient (proton motive force, PMF) that drives ATP synthesis ([1](#)). In ETCs, quinones and cytochromes are two types of electron carriers that shuttle electrons to and from large macromolecular structures embedded in the membrane. In the mitochondrial respiratory chain, four membrane oxidoreductases are involved in electron transfer: complex I (NADH:ubiquinone oxidoreductase, CI), complex II (succinate:ubiquinone oxidoreductase, CII), complex III (*bc*₁-type ubiquinol:cytochrome *c* oxidoreductase, *bc*₁-type CIII) and complex IV (*aa*₃-type cytochrome *c* oxidase, *aa*₃-type CIV). CIII oxidizes ubiquinol to ubiquinone and passes the electrons to soluble cytochrome *c* which then shuttles them to CIV, where oxygen is reduced to water (**Fig. 1A**). The transmembrane PMF is generated by proton pumping in CI, CIII and CIV.

The situation is more complicated in prokaryotic respiratory chains (**Fig. 1A**) ([2](#)). A soluble cytochrome *c* pathway similar to that in mitochondria is common in Gram-negative bacteria. Variations include a membrane-anchored cytochrome *c* mediating electron transfer from CIII to CIV ([3](#)) and a *caa*₃-type CIV with a fused cytochrome *c* domain ([4](#)). Gram-positive bacteria usually possess cytochrome *c* proteins that are anchored onto the membrane ([5](#)), or a fused cytochrome *c* domain (*bcc*-type CIII or *caa*₃-type CIV) to mediate electron transfer between CIII and CIV ([6](#), [7](#)). *Mycobacteria* and other *Actinobacteria* such as *Corynebacterium glutamicum* are inherently devoid of a soluble cytochrome *c* in their genomes ([8](#)), but contain a *bcc*-type CIII with a di-heme cytochrome *c* domain fused to CIII ([9](#), [10](#)). Variations are also observed within CIII and CIV. Alternative Complex IIIs (ACIIIs) which are structurally unrelated to *bc*₁-type CIII mediate quinol oxidation ([11](#)). Quinol oxidases couple quinol oxidation to oxygen reduction without the need for cytochrome *c* ([12](#)). Alternative oxidases (Aox) catalyze quinol oxidation/oxygen reduction without proton pumping ([13](#)).

Despite variation with ETCs, homologs or analogs of CI through to CIV are the most common components of respiratory chains in aerobic organisms. Structures of both prokaryotic and eukaryotic CI ([14-16](#)), CII ([17](#), [18](#)), CIII ([19-21](#)) and CIV ([22-24](#)) have been determined, elucidating the flow of electrons within these individual complexes. Structural information for the mitochondrial respirasome CI₁CIII₂CIV₁ and preliminary electron microscopic study of a CIII₂CIV₂ supercomplex from yeast have been reported ([25](#), [26](#)). However, cytochrome *c* is not

visible in any of these structures. Thus, a complete pathway for electron flow is yet to be fully elucidated. Understanding the precise details of the structural assembly for a CIII–CIV supercomplex will greatly assist in this endeavor (27, 28). It has been reported recently that respiratory supercomplexes *in situ* have a conserved core of CI and a dimer of CIII but otherwise their stoichiometry and structure vary (29). Up to two copies of monomeric CIV were found associated with the CI₁CIII₂ assembly in bovine heart and the yeast *Yarrowia lipolytica*, but their positions varied (30). The conserved features of supercomplex assemblies such as CI₁CIII₂ and CIII₂CIV₂ suggest that these types of associations have important roles in respiratory electron transfer.

The *bcc*-type CIII from *Actinobacteria* has a di-heme *c* subunit (7). It has been suggested that one cytochrome *c* domain is the donor for the *aa*₃-type CIV and the other is the acceptor for the CIII Rieske Fe-S protein (31). In support of this concept of intra-supercomplex electron transfer, CIII–CIV supercomplexes have been isolated from *M. smegmatis*, *C. glutamicum*, and *M. tuberculosis* and shown to couple quinol oxidation to oxygen reduction without an external electron shuttle (9, 10, 32). Therefore, structural data for the *bcc-aa*₃ type CIII–CIV supercomplex (SC III–IV) can provide answers as to how CIII and CIV are coupled and how electrons are transferred from CIII to CIV.

Purification and characterization of SC III–IV

To isolate the SC III–IV in a functional form, we engineered the genome of *M. smegmatis* to incorporate a 10× His tag at the C-terminus of the QcrB subunit of CIII, extracted and purified the CIII–CIV complex by Ni-NTA affinity chromatography and gel filtration. Gel filtration and Blue-Native PAGE showed a single peak and a single band, suggesting a highly-ordered supramolecular assembly (fig. S1, A and B). SDS-PAGE and mass spectrometry confirmed the presence of all the known components of CIII and CIV as well as several previously unknown components (fig. S1D and table S1). Native Orbitrap mass spectrometry gave a molecular weight of 873.4 kDa ± 10.4 Da for the complex (fig. S1E). Both the electronic absorption spectrum and the electron paramagnetic resonance (EPR) spectrum showed peaks expected from the various hemes, copper centers and [2Fe-2S] prosthetic groups in CIII and CIV (fig. S1K). Since the *bcc-aa*₃ preparations from *M. smegmatis* are active with the more soluble menadiol (2-methyl-1,4-naphthoquinol) as substrate (33), the quinol:oxygen oxidoreductase activity of SC III–IV was assayed by the rate of O₂ consumption in the presence of menadiol. SC III–IV oxidized menadiol and reduced O₂ with an apparent *k*_{cat} of 2.80 ± 0.05 s⁻¹ for O₂ consumption or 11.20 ± 0.20 e⁻ s⁻¹ and a *K*_m of 120.70 ± 3.72 μM for menadiol (fig. S2, A, B and C). The *k*_{cat} value is comparable to the 65 e⁻ s⁻¹ reported for this complex with 2,3-dimethyl-1,4-naphthoquinol (DMNQH₂) as the electron donor (9); the difference is likely due to DMNQH₂ being more reducing and a closer structural analogue of the natural substrate menaquinol than menadiol. The data confirm that the purified sample is a functioning supercomplex containing CIII and CIV and capable of directly coupling quinol oxidation to oxygen reduction.

Overall architecture of SC III–IV

The structure of SC III–IV was determined by cryo-EM to an overall resolution of 3.5 Å (Fig. 1B, table S2, fig. S3C and movie S1). The dimensions of the supercomplex are 200 × 70 × 120 Å, with a linear dimeric CIV₁–CIII₂–CIV₁ arrangement where individual CIVs flank the central CIII dimer on either side (Fig. 1, B and C, and movie 1). This C₂ symmetrized linear architecture is completely different from those previously reported for respiratory supercomplexes (fig. S4). CIII

is comprised of canonical three subunits as a homodimer (**Fig. 2A and fig. S5A**). In addition to the four known subunits of *M. smegmatis* CIV, two subunits were observed that match two of the newly identified proteins, CtaI and CtaJ (**Fig. 2B and fig. S3H**), showing a similar topology and binding schema to the subunit Va and IV in mitochondrial CIV (**fig. S5J**).

There is extra density within the interface between CIII and CIV as well as at the top of the CIII dimer (**Fig. 1B**). The density within the interface could be modeled by two proteins LpqE and PRSAF1 (prokaryotic respiratory supercomplex association factor 1, **Fig. 1C and movie 1**). LpqE was found to be a N-terminal triacylated lipoprotein (**Fig. 4F**), with a *N*-acylated-*S*-diacylated modification of Cys24 within the lipobox (–²¹Lxx²⁴C–) sequence ([34](#)). On the periplasmic side the density on top of the CIII dimer consisted of a peptide fragment linked with a region of bulk density which could be visualized in a low-pass filtered map. The peptide fragment was modeled with residues Cys21–Pro45 of the N-terminal sequence of superoxide dismutase SodC of *M. smegmatis*. The EM map indicated side chain modifications, including triacylation at Cys21 that was part of a lipobox (–¹⁸Lxx²¹C–) sequence (**Fig. 4E**) and possible glycosylation sites (**fig. S3H**). Native mass spectrometry further identified that SodC is a component of SC III–IV (**fig. S1F**). The stoichiometry of SodC was confirmed as a dimer through the collisional dissociation of the SodC complex. Extensive glycosylation and copper-binding of SodC was observed in the mass spectrum (**fig. S1F**). The bulk density was therefore fitted with a dimer of SodC (**Fig. 1B and 1C, and fig. S3F**). SC III–IV possesses superoxide dismutase activity, with a specific activity of 132.56 ± 12.57 IU/mg-SOD, assuming 100% occupancy (**fig. S2E**). SodC association with SC III–IV was also confirmed by isolation of the supercomplex by Ni-affinity chromatography when a His-tag was introduced only to the C-terminus of SodC and not any of the CIII and CIV subunits. The SodC-tagged form of the complex showed a higher specific activity of 957.36 ± 23.34 IU/mg-SOD but still lower than the 1000–6000 IU/mg-SOD typically observed with soluble SOD enzymes. It also indicates an ~14% (SodC)₂ occupancy in the purified QcrB-tagged SC III–IV particles for cryo-EM study. Thus, it appears that there might be some dissociation of SodC from SC III–IV during detergent solubilization. It is also possible that the SOD occupancy is growth regulated since an up-regulation of *sodC* (the gene encoding the SOD here) in response to phagocytosis by human macrophages has been reported ([35](#)). Further work on the role of SOD in association with SC III–IV is in progress.

All the prosthetic groups predicted from the canonical CIII and CIV subunits were clearly resolved and found to be coordinated with conserved canonical residues (**fig. S3J**). Two menaquinone (MK) molecules were observed at the quinone binding sites in CIII. The calculated molar ratio between iron atoms and copper atoms in the final model is 1.6, in excellent agreement with the value of 1.5 determined by atomic absorption spectroscopy (**fig. S1C**). SodC from *M. tb* does not contain zinc ([36](#)), and atomic absorption spectroscopy analysis showed that zinc was absent from SC III–IV (**fig. S1C**). We were also able to build 34 phospholipids (**fig. S3I**) and ten MK molecules in SC III–IV. The total molecular mass of the model, including the new identified subunits, is ~760 kDa which is lower than the $873.4 \text{ kDa} \pm 10.4 \text{ Da}$ determined by native Orbitrap mass spectrometry (**fig. S1E**). This difference may be accountable on the basis of contributions from the detergents/lipids and the possibility of the presence of additional unidentified subunits.

Structure of CIII and CIV in the supercomplex

The cryo-EM map clearly shows QcrA, QcrB and QcrC of CIII in a dimeric form with all their prosthetic groups visualized (**Fig. 2A, fig. S3, H and J, and movie 2**). QcrA has a “U” shaped

structure within its N-terminal domain while the equivalent subunit in *bc*₁-type CIII has only one TMH (equivalent to QcrA TMH3) (**Fig. 2A and fig. S5A**). The region linking the two arms is located near the cytoplasmic side. The C-terminal domain of QcrA TMH3 is on the periplasmic side and holds the [2Fe-2S] cluster. Importantly, QcrA here also has a roof-like structure on the periplasmic side which is involved in the dimerization of CIII (**Fig. 2A**) while the *bc*₁-type CIIIs do not have this feature. The heme *b*_H and heme *b*_L cofactors are bound within four TMHs in QcrB (**Fig. 2A**). The N-terminal periplasmic portion of QcrC can be divided into two heme-containing cytochrome *c* domains D1 and D2 (equivalent to the *c*₁ domain in *bc*₁ complex) (**Fig. 2A**). These two domains are in close contact with and face each other in an anti-parallel orientation. The D2 domain interacts extensively with QcrA and QcrB, while the additional D1 domain protrudes out of the core of CIII and is involved in direct intra-supercomplex electron transfer (see below). Overall, although the *bcc*-type CIII in the supercomplex shares a similar dimeric association as the bacterial *bc*₁-type CIII and mitochondrial CIII, the structural details are markedly different (**fig. S5B**).

CIV in SC III–IV belongs to the type A heme-copper oxidase (HCO) family (**Fig. 2B and movie 3**) ([37](#)). The central cavity of the barrel-like arrangement of the 12 TMHs in the CtaD subunit holds heme *a*, heme *a*₃ and Cu_B. The C-terminal hydrophilic β barrel domain of CtaC holds the two Cu_A ions. The four protons required for oxygen reduction by heme *a*₃:Cu_B in CIVs are transferred to the catalytic center through two pathways denoted D and K ([38](#)). Due to the limited resolution, water molecules are not observed in our model. However, structure comparison revealed that the D and K pathways are conserved in SC III–IV (**fig. S5, K and L**).

Interaction between CIII and CIV and the contribution of association subunits and lipids

The linear form of SC III–IV arises from the dimerization of CIII which is mediated by contacts between subunits QcrA and QcrB (**Fig. 2A, fig. S6**). There are extensive contacts between CIII and CIV on both the cytoplasmic and periplasmic sides of the membrane (**Fig. 3**). Of the three association subunits LpqE, PRSAF1 and SOD in SC III–IV, both LpqE and PRSAF1 form numerous contacts with CIII and CIV, suggesting an important role for both in supercomplex stability (**Fig. 3B and fig. S6, E to G**). SOD utilizes its lipid-modified N-terminal fragment to associate with CIII (**Fig. 4E**) and forms a dimer on the periplasmic side of the CIII dimer. There are no direct interactions between the main body of the SOD dimer and CIII or CIV. This might allow a flexible orientation for this subunit which could be important for efficient clearance of ROS generated by side reactions when electrons are transferred from CIII to CIV (see below).

Phospholipids, especially cardiolipin (CL), are known to contribute to both the assembly and stability of respiratory complexes and supercomplexes ([39](#)). In the structure of SC III–IV, phospholipids are identified in the transmembrane space of CIII and CIV and the interface between CIII and CIV (**Fig. 4**). Of particular note are the four CL molecules in the large groove between CIII and CIV (**Fig. 4D**); the sixteen fatty acid chains fill most of the space in the groove and may play an important role in stabilizing the supercomplex. The N-terminal modified lipid tails of the lipoproteins SOD and LpqE mediate inter-subunit hydrophobic interactions and contribute to the stability of the supercomplex (**Fig. 4E and fig. 4F**). These lipid modifications described here are similar to those observed in a recently described structure of alternative complex III ([11](#)).

Quinone and quinone binding pockets

Quinone binding sites of respiratory complexes are of great interest because they are part of the Q-cycle hypothesis. They have varied sequences and specificities between species, and are often

the sites for inhibitor binding and thus are important for drug discovery. We have identified the two quinone binding sites (Q_P and Q_N) in SC III–IV (**Fig. 5**). The quinol oxidation site (Q_P site) responsible for menaquinol (MKH₂) oxidation is near heme b_L while the quinone reduction site (Q_N site) responsible for menaquinone (MK) reduction is close to heme b_H .

The Q_P site near heme b_L is at the center of an inverted triangle structure and surrounded by helices (**Fig. 5A**). Residues at this site are not conserved compared to the bc_1 complex (**Fig. 5C**). The typical “PEWY” motif in the bc_1 complex is replaced by “PDFY” (**fig. 5C**). One MK molecule is identified at this site with its naphthoquinone ring surrounded mainly by hydrophobic residues. The edge-to-edge distance from MK to heme b_L is 16 Å. Thus, we speculate that the endogenous electron donor MKH₂ would bind closer to heme b_L to facilitate electron transfer and what we observe here might be a representation of the oxidized product as it leaves the Q_P site. Furthermore, there are no observed hydrogen bonds to the carbonyl groups of MK (**Fig. 5A**). It is known that proton abstraction from MKH₂ is coupled to electron donation to CIII. Thus, hydrogen bonds are needed between the binding residues and the hydroxyl group of MKH₂ to help deprotonate the substrate. Hence MKH₂ should bind deeper inside the pocket, close to polar residues such as Q_{crB} Tyr159, Q_{crB} Thr308, Q_{crB} Asp309 (**Fig. 5A**). Structural superposition with the inhibitor bound bc_1 complex (40) shows that the MK at the Q_P site binds deeper into the pocket in the bc_1 complex than in this SC III–IV complex.

By contrast, the head group of MK at the Q_N site is bound in a similar fashion to ubiquinone in the structures of bc_1 complexes (**Fig. 5B**). As found for the Q_P site, these residues are not conserved compared to the bc_1 complexes from bacteria to eukaryotes (**Fig. 5C**). In particular, the carbonyl groups of ubiquinone are coordinated by the conserved His and Asp amongst bc_1 complexes; these residues are substituted by Q_{crB} Trp231 and Q_{crB} Ser261 in the bcc -type CIII of *M. smegmatis*. The carbonyl groups of MK in SC III–IV interact with the side chains of Q_{crB} Tyr48 and Q_{crB} Ser261 that may supply protons for MK reduction. The MK head group is ideally placed for electron transfer, being within 5 Å of the A-edge of heme b_H .

Besides finding quinone molecules at the Q sites, we also observed map signals for another three possible MK/MKH₂ molecules in the supercomplex (**fig. S7, C to E**). However, further experiments are needed to clarify the identity and function of these molecules.

The new family of candidate anti-mycobacterials, the imidazo[1,2-a]pyridines (IP) represented by Q203 operate by competing with menaquinone for binding at the Q_P site of CIII of *M. tuberculosis* (41). Sequence alignments indicate a high similarity between the Q_P sites of CIIIs from *M. tuberculosis* and *M. smegmatis* (**fig. 5C**), thus suggesting Q203 would also have a similar binding mechanism and a similar effect on the activity of *M. smegmatis* CIII. Indeed, recent studies of the anti-mycobacterial activity of Q203 on *M. tuberculosis* and *M. smegmatis* demonstrated that Q203 targets the bcc complex in both with similar affinity (42). We investigated the *in vitro* inhibition of *M. smegmatis* SC III–IV by Q203 by the menadiol/oxygen oxidoreductase activity assay and compared the effect with a hybrid supercomplex of *M. tuberculosis* bcc -CIII and *M. smegmatis* aa_3 -CIV. Q203 showed inhibition of menadiol-induced oxygen consumption with IC₅₀ values of 0.84 ± 0.22 μM and 0.61 ± 0.16 μM for SC III–IV and the hybrid supercomplex, respectively (**fig. S2D**).

Prosthetic groups and implication for direct electron transfer

The prosthetic groups of CIII (heme b_H/b_L , [2Fe-2S] clusters and heme c_{D1}/c_{D2}) and CIV (Cu_A,

Cu_B and heme *a/a*₃) are clearly identified from the cryo-EM map (**Fig. 2, A and B, and fig. S3J**). The redox centers in CIII and CIV are within distances that allow long-range electron transfer (**Fig. 6A**). Both heme *b*_L and heme *b*_H are found in QcrB_{CIII} (**fig. S3J and fig. S8A**). The edge-to-edge distance between the two heme groups is 12 Å, allowing rapid inter-heme electron transfer. The shortest distance from *b*_L to MK at the Q_P site and from *b*_H to MK at the Q_N site are 16 Å and 5 Å, respectively (**Fig. 6A**). Previous studies have proposed that CIIIs from different species adopt a dimeric architecture and form a H-shaped electron transfer system that distributes electrons between four quinone oxidation-reduction sites within the CIII dimer (43). Consistent with this hypothesis, upon dimerization of *M. smegmatis* CIII, the two *b*_L heme groups from the CIII monomers are 14 Å apart (**Fig. 6A**), allowing electron tunneling between the two hemes.

The heme *c*_{D1}-containing D1 domain of QcrC_{CIII} protrudes into the periplasm and interacts with the Cu_A-containing periplasmic domain of CtaC_{CIV} (**Fig. 6A**). The edge-to-edge distance from heme *c*_{D1} to the Cu_A centre is 12 Å. At the interface between these two domains there is a gating residue CtaC_{Trp138} on the Cu_A binding loop. The distance between CtaC_{Trp138} and the Cu_A center and that between CtaC_{Trp138} and heme *c*_{D1} are approximately equal. It has been proposed, based on mutagenesis studies, that the corresponding Trp121 (44) of *P. denitrificans* CIV is the electron entry site from cytochrome *c*. CIVs from *B. taurus* also possesses a tryptophan residue at the equivalent location (45). Thus, the heme *c*_{D1}-containing D1 domain of QcrC_{CIII} here interacts with CIV on a similar electron entry site as in other respiratory complexes.

Within CIV, the heme *a* group is just below the Cu_A center and the heme *a*₃ group is beside heme *a* (**Fig. 6A**). Cu_B is coordinated to three conserved His residues. The space between the iron of heme *a*₃ and Cu_B is the catalytic center for reduction of oxygen. In proximity to propionate groups of heme *a*₃, a Cu_C ion was modeled according to the cryo-EM map (**fig. S3J**). In other reported CIV structures the equivalent density at this site is occupied by a water molecule (46) or a Mg²⁺ ion (47). However, we did not detect magnesium in our AAS analysis (**fig. S1C**). The edge-to-edge distance between Cu_C and the Cu_A center and that between Cu_C and heme *a*₃ are 12 Å and 9 Å, respectively.

From the positions of the prosthetic groups in *M. smegmatis* SC CIII₂CIV₂SOD₂ and the redox center separations, it is possible to trace an uninterrupted pathway for the flow of electrons within the supercomplex starting from the electron donor at the Q_P site in CIII to the final site of oxygen reduction in CIV (**Fig. 6B**). Menaquinol (MKH₂) from the Q-pool binds at the Q_P site near heme *b*_L and transfers one electron to the [2Fe-2S] cluster and the other to heme *b*_L which passes the electron *via* heme *b*_H to a menaquinone (MK) bound at the Q_N site, generating the highly reactive intermediate menasemiquinone (MK•). The reduced [2Fe-2S] cluster is within electron tunneling distance to transfer an electron to heme *c*_{D2} which rapidly passes the electron to heme *c*_{D1}. A second MKH₂ then binds at the Q_P site and repeats the process. The MK• at the Q_N site is fully reduced to MKH₂ and released to the Q-pool. This completes the Q cycle. An electron path between CIIIs in the dimer is also possible through tunneling between the adjacent *b*_L heme groups, albeit with low efficiency (43). The reduced [2Fe-2S] cluster again transfers the other electron to heme *c*_{D2}/*c*_{D1}. Once heme *c*_{D1} is reduced, two Cu_A ions of CtaC_{CIV} accept the electron through contacts forged with the D1 domain of QcrC_{CIII}. At this point, an electron is transferred from CIII to CIV. Within CIV, the electron is transferred through heme *a* (or possibly the Cu_C center) and finally reaches the terminal heme *a*₃:Cu_B reaction center for oxygen reduction. As a consequence of the electron transfer, protons are translocated to the periplasm, forming a transmembrane PMF. Throughout the entire pathway from the Q_P site to the terminal oxygen reduction center, electrons

tunnel between prosthetic groups that are all buried inside this integral complex.

Quinone reduction at the Q_N site to complete the Q cycle can be bypassed/short-circuited if both electrons from MKH_2 oxidation at the Q_P site are transferred to the [2Fe-2S] cluster and then to CIV for oxygen reduction. Hence, competent energy transduction requires that electron transfer from the Q_P site has to be bifurcated between reduction of the [2Fe-2S] cluster and heme b_L . In essence, the pathway for transferring electrons from the [2Fe-2S] cluster eventually to CIV has to be sufficiently slow for electron transfer to the Q_N site for quinone reduction to occur. In the bc_1 complex the [2Fe-2S] cluster domain cycles between “ b ” and “ c_1 ” states. In the b -state the [2Fe-2S] cluster is close to the Q_P site to accept an electron from quinol oxidation but too far away (26 Å, **figure S5E**) to transfer an electron to the c_1 heme at an appreciable rate. The cluster domain undergoes a “head displacement” conformation change to the c_1 -state where the [2Fe-2S] cluster moves to within 11 Å of the c_1 heme to facilitate electron transfer. This head displacement or “gating” step occurs with a rate constant of $6 \times 10^4 \text{ s}^{-1}$ (48).

We cannot rule out the possibility that SC III–IV could adopt a different conformation and cycle between states similar to the b and c_1 states of bc_1 complexes. However, the dimer of QcrA is held firmly in place by the periplasmic roof-like structure and further surrounded by QcrB and QcrC, which might limit the space for the potential conformational change (**fig. S5D**). Structural superposition shows that the position of the [2Fe-2S] in QcrA is similar to that of bc_1 -type CIII in the b state, i.e. rapid cluster reduction by MKH_2 can occur. The [2Fe-2S] cluster is at a distance of 16 Å from heme c_{D2} . We used this distance, the reported midpoint potentials of the prosthetic groups (10), and a reorganization energy (λ) of 0.7 eV to calculate a rate constant of electron transfer of $5.6 \times 10^2 \text{ s}^{-1}$ from [2Fe-2S] to heme c_{D2} (49). This is much slower than the head displacement gating step in bc_1 complexes ($6 \times 10^4 \text{ s}^{-1}$). We conclude that short-circuiting in SC III–IV is likely to be rate-limited by slow electron transfer between the [2Fe-2S] cluster and heme c made possible by positioning of the chain of redox centers, rather than by conformational changes as found in bc_1 complexes.

Role of SOD association

In aerobic organisms, the respiratory ETC not only generates the energy needed to fuel biological functions but is also a major source of intracellular ROS that can cause damage to cellular structures and components (50). Complex III is one of the major sites of ROS production (51). While ROS are emerging as important elements in the bacterial response to lethal stress (52), it is well documented that they can disturb respiratory activity via oxidative damage of ETC complexes which are in turn protected by the ROS scavengers SOD and catalase (53–55). Up-regulation of *M. tuberculosis* *sodC* (the gene encoding the SOD here) in response to phagocytosis by human macrophages has been observed (35). This Mycobacterial Cu, Zn superoxide dismutase SodC was identified as a membrane-bound enzyme and proposed to protect specific membrane-associated targets from oxy-radical damage, thus facilitating mycobacterial intracellular growth (35). A null *sodC* mutant of *M. tuberculosis* was shown to be readily killed by externally generated superoxide and by activated macrophages producing oxidative bursts (56). In this work, we found that catalytically active SodC is an integral part of a respiratory supercomplex $CIII_2CIV_2SOD_2$. SodC could serve to scavenge ROS generated locally or by other ETC complexes, as well as ROS released by the immune response of the host. Its recruitment has the potential to make this critical respiratory machinery a robust system even under the high oxidative stress inside macrophages. Immunoblotting of *Caenorhabditis elegans* respiratory supercomplexes separated by BN-PAGE

showed that mitochondrial superoxide dismutase-2 (mtSOD-2) is associated with the respirasome CI–CIII₂–CIV, suggesting that the mtSOD might also provide similar local protection against ROS damage (57).

Conclusions

The cryo-EM structure of a CIII–CIV respiratory supercomplex from *M. smegmatis* has revealed a complete intra-complex electron transfer pathway from quinol oxidation in CIII to oxygen reduction in CIV, a new mechanism for bifurcating electron transfer to ensure completion of the Q cycle for energy transduction, and the association of a superoxide dismutase that can provide protection against oxidative damage by reactive oxygen species. The structure of the quinone binding sites also provide a framework for structure-based anti-mycobacterial drug discovery.

References:

1. P. Mitchell, Coupling of phosphorylation to electron and hydrogen transfer by a chemi-osmotic type of mechanism. *Nature* **191**, 144-148 (1961).
2. A. M. Melo, M. Teixeira, Supramolecular organization of bacterial aerobic respiratory chains: From cells and back. *Biochim Biophys Acta* **1857**, 190-197 (2016).
3. E. A. Berry, B. L. Trumpower, Isolation of ubiquinol oxidase from *Paracoccus denitrificans* and resolution into cytochrome bc₁ and cytochrome c-aa₃ complexes. *J Biol Chem* **260**, 2458-2467 (1985).
4. J. A. Fee, M. G. Choc, K. L. Findling, R. Lorence, T. Yoshida, Properties of a copper-containing cytochrome c₁aa₃ complex: a terminal oxidase of the extreme thermophile *Thermus thermophilus* HB8. *Proc Natl Acad Sci U S A* **77**, 147-151 (1980).
5. J. Bengtsson, C. Rivolta, L. Hederstedt, D. Karamata, *Bacillus subtilis* contains two small c-type cytochromes with homologous heme domains but different types of membrane anchors. *J Biol Chem* **274**, 26179-26184 (1999).
6. M. Saraste *et al.*, The *Bacillus subtilis* cytochrome-c oxidase. Variations on a conserved protein theme. *Eur J Biochem* **195**, 517-525 (1991).
7. N. Sone *et al.*, A novel hydrophobic diheme c-type cytochrome. Purification from *Corynebacterium glutamicum* and analysis of the QcrCBA operon encoding three subunit proteins of a putative cytochrome reductase complex. *Biochim Biophys Acta* **1503**, 279-290 (2001).
8. S. T. Cole *et al.*, Deciphering the biology of *Mycobacterium tuberculosis* from the complete genome sequence. *Nature* **393**, 537-544 (1998).
9. J. A. Megehee, J. P. Hosler, M. D. Lundrigan, Evidence for a cytochrome bcc-aa₃ interaction in the respiratory chain of *Mycobacterium smegmatis*. *Microbiology* **152**, 823-829 (2006).
10. W. C. Kao *et al.*, The obligate respiratory supercomplex from Actinobacteria. *Biochim Biophys Acta* **1857**, 1705-1714 (2016).
11. C. Sun *et al.*, Structure of the alternative complex III in a supercomplex with cytochrome oxidase. *Nature* **557**, 123-126 (2018).
12. A. Puustinen, M. Finel, T. Haltia, R. B. Gennis, M. Wikstrom, Properties of the two terminal oxidases of *Escherichia coli*. *Biochemistry* **30**, 3936-3942 (1991).
13. Anthony L. Moore, Mary S. Albury, Further insights into the structure of the alternative oxidase: from plants to parasites. *Biochemical Society Transactions* **36**, 1022-1026 (2008).

14. R. Baradaran, J. M. Berrisford, G. S. Minhas, L. A. Sazanov, Crystal structure of the entire respiratory complex I. *Nature* **494**, 443-448 (2013).
15. K. R. Vinothkumar, J. Zhu, J. Hirst, Architecture of mammalian respiratory complex I. *Nature* **515**, 80-84 (2014).
16. J. Zhu, K. R. Vinothkumar, J. Hirst, Structure of mammalian respiratory complex I. *Nature* **536**, 354-358 (2016).
17. V. Yankovskaya *et al.*, Architecture of succinate dehydrogenase and reactive oxygen species generation. *Science* **299**, 700-704 (2003).
18. F. Sun *et al.*, Crystal structure of mitochondrial respiratory membrane protein complex II. *Cell* **121**, 1043-1057 (2005).
19. D. Xia *et al.*, Crystal structure of the cytochrome bc₁ complex from bovine heart mitochondria. *Science* **277**, 60-66 (1997).
20. S. Iwata *et al.*, Complete structure of the 11-subunit bovine mitochondrial cytochrome bc₁ complex. *Science* **281**, 64-71 (1998).
21. Z. Zhang *et al.*, Electron transfer by domain movement in cytochrome bc₁. *Nature* **392**, 677-684 (1998).
22. S. Iwata, C. Ostermeier, B. Ludwig, H. Michel, Structure at 2.8 Å resolution of cytochrome c oxidase from *Paracoccus denitrificans*. *Nature* **376**, 660-669 (1995).
23. T. Tsukihara *et al.*, The whole structure of the 13-subunit oxidized cytochrome c oxidase at 2.8 Å. *Science* **272**, 1136-1144 (1996).
24. S. Yoshikawa *et al.*, Redox-coupled crystal structural changes in bovine heart cytochrome c oxidase. *Science* **280**, 1723-1729 (1998).
25. J. A. Letts, K. Fiedorczuk, L. A. Sazanov, The architecture of respiratory supercomplexes. *Nature* **537**, 644-648 (2016).
26. E. Mileykovskaya *et al.*, Arrangement of the respiratory chain complexes in *Saccharomyces cerevisiae* supercomplex III₂IV₂ revealed by single particle cryo-electron microscopy. *J Biol Chem* **287**, 23095-23103 (2012).
27. J. A. Letts, L. A. Sazanov, Clarifying the supercomplex: the higher-order organization of the mitochondrial electron transport chain. *Nat Struct Mol Biol* **24**, 800-808 (2017).
28. D. Milenkovic, J. N. Blaza, N. G. Larsson, J. Hirst, The Enigma of the Respiratory Chain Supercomplex. *Cell Metab* **25**, 765-776 (2017).
29. J. D. Chavez *et al.*, Chemical Crosslinking Mass Spectrometry Analysis of Protein Conformations and Supercomplexes in Heart Tissue. *Cell Syst* **6**, 136-141 e135 (2018).
30. K. M. Davies, T. B. Blum, W. Kuhlbrandt, Conserved in situ arrangement of complex I and III₂ in mitochondrial respiratory chain supercomplexes of mammals, yeast, and plants. *Proc Natl Acad Sci U S A* **115**, 3024-3029 (2018).
31. A. Niebisch, M. Bott, Molecular analysis of the cytochrome bc₁-aa₃ branch of the *Corynebacterium glutamicum* respiratory chain containing an unusual diheme cytochrome c₁. *Arch Microbiol* **175**, 282-294 (2001).
32. M. S. Kim *et al.*, Isolation and characterization of a hybrid respiratory supercomplex consisting of *Mycobacterium tuberculosis* cytochrome bcc and *Mycobacterium smegmatis* cytochrome aa₃. *J Biol Chem* **290**, 14350-14360 (2015).
33. E. Lemma, H. Schagger, A. Kroger, The menaquinol oxidase of *Bacillus subtilis* W23. *Arch Microbiol* **159**, 574-578 (1993).
34. M. M. Babu *et al.*, A database of bacterial lipoproteins (DOLOP) with functional assignments to predicted lipoproteins. *J Bacteriol* **188**, 2761-2773 (2006).

35. M. D'Orazio *et al.*, Lipid modification of the Cu,Zn superoxide dismutase from *Mycobacterium tuberculosis*. *Biochem J* **359**, 17-22 (2001).
36. L. Spagnolo *et al.*, Unique features of the sodC-encoded superoxide dismutase from *Mycobacterium tuberculosis*, a fully functional copper-containing enzyme lacking zinc in the active site. *J Biol Chem* **279**, 33447-33455 (2004).
37. F. L. Sousa *et al.*, The superfamily of heme-copper oxygen reductases: types and evolutionary considerations. *Biochim Biophys Acta* **1817**, 629-637 (2012).
38. M. Svensson-Ek *et al.*, The X-ray crystal structures of wild-type and EQ(I-286) mutant cytochrome c oxidases from *Rhodobacter sphaeroides*. *J Mol Biol* **321**, 329-339 (2002).
39. A. Magalon, R. Arias-Cartin, A. Walburger, Supramolecular organization in prokaryotic respiratory systems. *Adv Microb Physiol* **61**, 217-266 (2012).
40. D. Birth, W. C. Kao, C. Hunte, Structural analysis of atovaquone-inhibited cytochrome bc1 complex reveals the molecular basis of antimalarial drug action. *Nat Commun* **5**, 4029 (2014).
41. K. Pethe *et al.*, Discovery of Q203, a potent clinical candidate for the treatment of tuberculosis. *Nat Med* **19**, 1157-1160 (2013).
42. P. Lu *et al.*, The anti-mycobacterial activity of the cytochrome bcc inhibitor Q203 can be enhanced by small-molecule inhibition of cytochrome bd. *Sci Rep* **8**, 2625 (2018).
43. M. Swierczek *et al.*, An electronic bus bar lies in the core of cytochrome bc1. *Science* **329**, 451-454 (2010).
44. H. Witt, F. Malatesta, F. Nicoletti, M. Brunori, B. Ludwig, Tryptophan 121 of subunit II is the electron entry site to cytochrome-c oxidase in *Paracoccus denitrificans*. Involvement of a hydrophobic patch in the docking reaction. *J Biol Chem* **273**, 5132-5136 (1998).
45. S. Shimada *et al.*, Complex structure of cytochrome c-cytochrome c oxidase reveals a novel protein-protein interaction mode. *EMBO J* **36**, 291-300 (2017).
46. T. Soulimane *et al.*, Structure and mechanism of the aberrant ba(3)-cytochrome c oxidase from *thermus thermophilus*. *EMBO J* **19**, 1766-1776 (2000).
47. C. Ostermeier, A. Harrenga, U. Ermler, H. Michel, Structure at 2.7 Å resolution of the *Paracoccus denitrificans* two-subunit cytochrome c oxidase complexed with an antibody FV fragment. *Proc Natl Acad Sci U S A* **94**, 10547-10553 (1997).
48. F. Millett, B. Durham, Chapter 5 Use of ruthenium photooxidation techniques to study electron transfer in the cytochrome bc1 complex. *Methods Enzymol* **456**, 95-109 (2009).
49. C. C. Moser, J. M. Keske, K. Warncke, R. S. Farid, P. L. Dutton, Nature of biological electron transfer. *Nature* **355**, 796-802 (1992).
50. S. Bhattacharya, *Reactive Oxygen Species and Cellular Defense System*. (2015), pp. 17-29.
51. J. F. Turrens, A. Boveris, Generation of superoxide anion by the NADH dehydrogenase of bovine heart mitochondria. *Biochem J* **191**, 421-427 (1980).
52. X. Zhao, K. Drlica, Reactive oxygen species and the bacterial response to lethal stress. *Curr Opin Microbiol* **21**, 1-6 (2014).
53. G. Petrosillo, F. M. Ruggiero, N. Di Venosa, G. Paradies, Decreased complex III activity in mitochondria isolated from rat heart subjected to ischemia and reperfusion: role of reactive oxygen species and cardiolipin. *FASEB J* **17**, 714-716 (2003).
54. G. Paradies, G. Petrosillo, M. Pistolese, F. M. Ruggiero, The effect of reactive oxygen species generated from the mitochondrial electron transport chain on the cytochrome c oxidase activity and on the cardiolipin content in bovine heart submitochondrial particles.

- FEBS Lett* **466**, 323-326 (2000).
55. G. Paradies, G. Petrosillo, V. Paradies, F. M. Ruggiero, Oxidative stress, mitochondrial bioenergetics, and cardiolipin in aging. *Free Radic Biol Med* **48**, 1286-1295 (2010).
 56. D. L. Piddington *et al.*, Cu,Zn superoxide dismutase of *Mycobacterium tuberculosis* contributes to survival in activated macrophages that are generating an oxidative burst. *Infect Immun* **69**, 4980-4987 (2001).
 57. W. Suthammarak, B. H. Somerlot, E. Opheim, M. Sedensky, P. G. Morgan, Novel interactions between mitochondrial superoxide dismutases and the electron transport chain. *Aging Cell* **12**, 1132-1140 (2013).
 58. X. Li, F. Liu, Y. Hu, K. Mi, Draft genome sequence of mc² 51, a highly hydrogen peroxide-resistant *Mycobacterium smegmatis* mutant strain. *Genome Announc* **2**, (2014).
 59. I. Wittig, H. Braun, H. Schagger, Blue native PAGE. *Nature Protocols* **1**, 418-428 (2006).
 60. I. Wittig, H. Schagger, Features and applications of blue-native and clear-native electrophoresis. *Proteomics* **8**, 3974-3990 (2008).
 61. L. Y. J. G. M. De Oca *et al.*, The composition of the *Bacillus subtilis* aerobic respiratory chain supercomplexes. *Journal of Bioenergetics and Biomembranes* **44**, 473-486 (2012).
 62. S. M. Lam *et al.*, Extensive characterization of human tear fluid collected using different techniques unravels the presence of novel lipid amphiphiles. *J Lipid Res* **55**, 289-298 (2014).
 63. G. Shui *et al.*, Mycolic acids as diagnostic markers for tuberculosis case detection in humans and drug efficacy in mice. *EMBO Mol Med* **4**, 27-37 (2012).
 64. L. Lim *et al.*, Lanosterol induces mitochondrial uncoupling and protects dopaminergic neurons from cell death in a model for Parkinson's disease. *Cell Death Differ* **19**, 416-427 (2012).
 65. S. Graf *et al.*, Rapid electron transfer within the III-IV supercomplex in *Corynebacterium glutamicum*. *Sci Rep* **6**, 34098 (2016).
 66. J. M. McCord, I. Fridovich, Superoxide dismutase. An enzymic function for erythrocuprein (hemocuprein). *J Biol Chem* **244**, 6049-6055 (1969).
 67. D. N. Mastronarde, Automated electron microscope tomography using robust prediction of specimen movements. *J Struct Biol* **152**, 36-51 (2005).
 68. G. Tang *et al.*, EMAN2: an extensible image processing suite for electron microscopy. *J Struct Biol* **157**, 38-46 (2007).
 69. S. H. Scheres, Semi-automated selection of cryo-EM particles in RELION-1.3. *J Struct Biol* **189**, 114-122 (2015).
 70. S. H. Scheres, A Bayesian view on cryo-EM structure determination. *J Mol Biol* **415**, 406-418 (2012).
 71. S. H. Scheres, RELION: implementation of a Bayesian approach to cryo-EM structure determination. *J Struct Biol* **180**, 519-530 (2012).
 72. D. Kimanius, B. O. Forsberg, S. H. Scheres, E. Lindahl, Accelerated cryo-EM structure determination with parallelisation using GPUs in RELION-2. *Elife* **5**, (2016).
 73. X. Li *et al.*, Electron counting and beam-induced motion correction enable near-atomic-resolution single-particle cryo-EM. *Nat Methods* **10**, 584-590 (2013).
 74. S. Q. Zheng *et al.*, MotionCor2: anisotropic correction of beam-induced motion for improved cryo-electron microscopy. *Nat Methods* **14**, 331-332 (2017).
 75. K. Zhang, Gctf: Real-time CTF determination and correction. *J Struct Biol* **193**, 1-12 (2016).

76. S. Chen *et al.*, High-resolution noise substitution to measure overfitting and validate resolution in 3D structure determination by single particle electron cryomicroscopy. *Ultramicroscopy* **135**, 24-35 (2013).
77. P. B. Rosenthal, R. Henderson, Optimal determination of particle orientation, absolute hand, and contrast loss in single-particle electron cryomicroscopy. *J Mol Biol* **333**, 721-745 (2003).
78. A. Kucukelbir, F. J. Sigworth, H. D. Tagare, Quantifying the local resolution of cryo-EM density maps. *Nat Methods* **11**, 63-65 (2014).
79. L. J. McGuffin, K. Bryson, D. T. Jones, The PSIPRED protein structure prediction server. *Bioinformatics* **16**, 404-405 (2000).
80. L. A. Kelley, S. Mezulis, C. M. Yates, M. N. Wass, M. J. Sternberg, The Phyre2 web portal for protein modeling, prediction and analysis. *Nat Protoc* **10**, 845-858 (2015).
81. P. Emsley, B. Lohkamp, W. G. Scott, K. Cowtan, Features and development of Coot. *Acta Crystallogr D Biol Crystallogr* **66**, 486-501 (2010).
82. P. D. Adams *et al.*, PHENIX: a comprehensive Python-based system for macromolecular structure solution. *Acta Crystallogr D Biol Crystallogr* **66**, 213-221 (2010).
83. J. Yang *et al.*, The I-TASSER Suite: protein structure and function prediction. *Nat Methods* **12**, 7-8 (2015).
84. E. F. Pettersen *et al.*, UCSF Chimera--a visualization system for exploratory research and analysis. *J Comput Chem* **25**, 1605-1612 (2004).
85. W. L. Delano, The PyMOL Molecular Graphics System. (2002).
86. N. Sone, Y. Yanagita, A cytochrome aa₃-type terminal oxidase of a thermophilic bacterium. Purification, properties and proton pumping. *Biochimica et Biophysica Acta (BBA) - Bioenergetics* **682**, 216-226 (1982).
87. B. Chance, in *Methods in Enzymology*. (Academic Press, 1957), vol. 4, pp. 273-329.
88. M. J. Sartain, J. T. Belisle, N-Terminal clustering of the O-glycosylation sites in the Mycobacterium tuberculosis lipoprotein SodC. *Glycobiology* **19**, 38-51 (2009).
89. L. Esser *et al.*, Hydrogen bonding to the substrate Is not required for rieske iron-sulfur protein docking to the quinol oxidation site of complex III. *J Biol Chem* **291**, 25019-25031 (2016).
90. J. Koepke *et al.*, High resolution crystal structure of Paracoccus denitrificans cytochrome c oxidase: new insights into the active site and the proton transfer pathways. *Biochim Biophys Acta* **1787**, 635-645 (2009).
91. L. Holm, L. M. Laakso, Dali server update. *Nucleic Acids Res* **44**, W351-355 (2016).
92. J. Felsenstein, PHYLIP - Phylogeny Inference Package (Version 3.2). *Cladistics* **5**, 164-166 (1989).
93. F. D. Ciccarelli *et al.*, Toward automatic reconstruction of a highly resolved tree of life. *Science* **311**, 1283-1287 (2006).
94. K. L. Smollett *et al.*, Experimental determination of translational start sites resolves uncertainties in genomic open reading frame predictions - application to Mycobacterium tuberculosis. *Microbiology* **155**, 186-197 (2009).

Acknowledgments: We would like to thank Jianchao Zhang, Yini Zhang and Dr. Lei Wang from Prof. Chih-Chen Wang's Research Group (National Laboratory of Biomacromolecules, Institute of Biophysics, CAS) for their technical support on Clark-type oxygen electrode and oxygen

consumption assay and Prof. Kaixia Mi (CAS Key Laboratory of Pathogenic Microbiology and Immunology, Institute of Microbiology, CAS) for sharing the strain *M. smegmatis* mc² 51. We are also grateful to Boling Zhu, Xiaojun Huang and Gang Ji from Center for Biological Imaging (CBI), Institute of Biophysics, CAS and staff members from National Center for Protein Science Shanghai (NCPSS) for their technical support on cryo-EM and Dr. Chao Peng from the Mass Spectrometry System of NCPSS for his technical support. We also thank Tongxin Niu from the HPC-Service Station in CBI and Xiaodong Jian and Xiangfei Meng from TianHe-1(A) at National Supercomputer Center in Tianjin for computational support. **Funding:** This work was supported by grants from the National Key Research and Development Program of China (Grant No. 2017YFC0840300), the Strategic Priority Research Program of the Chinese Academy of Sciences (Grant No. XDB08020200), the State Key Development Program for Basic Research of the Ministry of Science and Technology of China (973 Project Grant Nos. 2014CB542800, 2014CBA02003 to ZR and 2014CB910700 to FS), and the National Natural Science Foundation of China (Grant Nos. 813300237 and 81520108019). **Author contributions:** Z.R. conceived, initiated and coordinated the project. H.G., Ju.L. and S.W. purified the *M. smegmatis* SC III-IV supercomplex; H.G., Y.T. and Ju.L. characterized the spectroscopic features of the samples; Ji.L., H.Y., C.R., S.L. and G.S. performed mass spectrometry analysis and identified the contents of the complex; Y.T. and Q.W. set up the biochemical assays and measured the menadiol:O₂ oxidoreductase activity of the complex; H.G. measured the superoxide dismutase activity of the complex; L.Y. and C.T. performed the EPR experiments and data analysis; A.X. and Q.W. collected and processed cryo-EM data; Q.W. reconstructed the 3.5 Å resolution map and supervised cryo-EM structure determination; Q.W., A.X., R.G. and W.J. built and refined the structure model; Ju.L., Q.W., F.S., H.G., A.X., X.Y., Y.S., X.L., M.J., C.T., C.Y., B.J., Z.L., L.G., L.W. and Z.R. analyzed the structure and discussed the results and the manuscript was written by F.S., Q.W., Ju.L., W.J., A.X., H.G., R.G., Z.L., L.G., L.W. and Z.R. **Competing interests:** The authors declare no competing interests. L.W. is a founder and consultant of Oxford Biotrans Ltd., UK. Carol? **Data and materials availability:** All data are available in the manuscript or the supplementary material. The accession number for the 3D cryo-EM density map reported in this paper is EMD-9610. The PDB accession number for the coordinates of the CIII-CIV complex is 6ADQ.

Supplementary Materials:

Materials and Methods

Figures S1-S8

Tables S1-S4

Movies S1

References 58-94

Figure Legends:

Fig. 1. Respiration in *Actinomycetes* and overall architecture of the Mycobacterial respiratory machine CIII₂CIV₂SOD₂. (A) The respiratory electron transfer chain in *Actinomycetes* (left) and the five major prokaryotic cytochrome *c* pathway variants with the organization schemes in representative organisms (right). The *M. smegmatis* cytochrome *c*

pathway has its cytochrome *c* fused with complex III, forming a *bcc*-type complex III that interacts with the *aa*₃-type complex IV to assemble into a CIII–CIV supercomplex. MK=menaquinone/menaquinol. (B) Overall architecture of the *bcc-aa*₃ type respiratory CIII–CIV supercomplex from *M. smegmatis*. The cryo-EM map of the supercomplex shows a linear two-fold dimerized form of CIV₁–CIII₂–CIV₁ with dimensions 200 × 70 × 120 Å. CIII is colored in orange, CIV in magenta and the association factors, PRSAF1 in green, LpqE in blue and SOD in grey. (C) Cartoon representation of the side view of the supercomplex (top) and a cross sectional view (bottom). The menaquinone/menaquinol (MK) is presented as bright green colored solid spheres and the phospholipids as yellow sticks. In the cross-sectional view (bottom), the boundaries of CIII, CIV and the association factor PRSAF1 are depicted with dashed lines in color (orange for CIII, magenta for CIV and green for PRSAF1).

Fig. 2. Structure of CIII₂ and CIV from *M. smegmatis*. (A) Overall structure of the CIII dimer (left) and the spatial location (right) of prosthetic groups. QcrA, QcrB and QcrC are colored pink, blue and gold, respectively. The two-fold symmetry of the dimer is depicted by the black axis. The zoom-in view shows the heme *c* binding domains (D1 and D2) of QcrC. The heme groups (*b*_H, *b*_L, *c*_{D1}, and *c*_{D2}) and [2Fe-2S] clusters are shown as spheres and menaquinone/menaquinol (MK) are shown as sticks. The regions of ridge roof, ceiling junction, and base plate of CIII dimer are marked with dashed ellipses. (B) Overall structure of CIV (left) and the spatial location (right) of prosthetic groups. CtaC, CtaD, CtaE, CtaF, CtaI and CtaJ are colored in magenta, dark green, yellowish brown, cyan, brown and violet, respectively. Prosthetic groups are shown as spheres.

Fig. 3. Interaction between CIII and CIV and roles of association subunits. (A) A section profile of the interaction interface between CIII and CIV. The left/right images show the surface of CIII/CIV and the bound structural segments from CIV/CIII subunits and the association subunits, LpqE and PRSAF1. (B) Interactions between the association subunits (PRSAF1, LpqE and SOD) and the subunits of CIII and CIV. The corresponding subunits of CIII and CIV are shown in surface representation and colored as indicated. The association subunits are shown in ribbon and colored as indicated. The catalytic domain of SOD was fitted in map and shown as a dimer (SOD₂). The lipid modification of SOD is shown in yellow sticks (see fig. 4E for detail).

Fig. 4. Important roles of phospholipids in the stability and assembly of the supercomplex. (A) The distribution of phospholipids in the membrane region (middle, view from periplasmic side) at the junction between the CIII monomers (left) and the interfaces between CIII and CIV (right). (B) A PE molecule mediates the interaction between PRSAF1 (TMH2) and CIV (CtaC and CtaD). (C) A PI molecule binds to the interface between QcrC TMH1 and CtaF TMH4. (D) Four CL molecules are bound in the groove between the TM regions of CIII and CIV (E) The N-terminal lipid modification of SOD at Cys21 binds to QcrB *via* hydrophobic interactions. (F) The N-terminal lipid modification of LpqE at Cys24 mediates the interactions between CtaD and PRSAF1.

Fig. 5. Structures of the menaquinone (MK)/menaquinol (MKH₂) binding sites in *M. smegmatis* CIII. (A) The Q_P binding site. (B) The Q_N binding site. The residues potentially involved in the binding of MK/MKH₂ are shown with side chains in a stick representation. The MK molecules are colored in green. The heme and [2Fe-2S] groups are shown in spheres and labeled accordingly. (C) Sequence alignment for the Q_P site and Q_N site in QcrB with other *Actinobacteria* and *Homo sapiens* ETC systems. The red and green dots indicate whether *Homo sapiens* shares a common conservative site with *Actinobacteria* (red) or not (green).

Fig. 6. The complete electron transfer pathway in the *bcc-aa*₃ type respiratory CIII/CIV supercomplex. (A) The prosthetic groups in the supercomplex are shown in sticks or spheres and

labeled accordingly with the corresponding midpoint potentials shown in brackets. These values are based on the measurement of that of the *bcc-aa₃* type supercomplex from *C. glutamicum* ([10](#)). The edge-to-edge distances between adjacent prosthetic groups are shown in black dashed lines with the numbers in the brackets representing the center-to-center distances. **(B)** A schematic diagram showing the entire electron transfer pathway from CIII to CIV and the relevant proton translocations in CIII and CIV. The potential role of associated SOD for the clearance of ROS is also proposed.

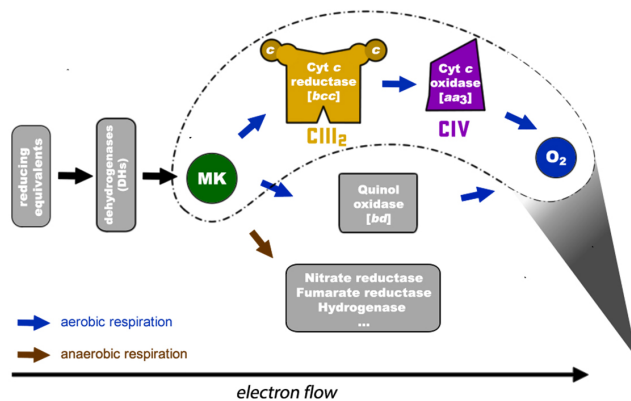
Movie 1. The overall architecture of the supercomplex. Cartoon representation of the supercomplex. The menaquinone/menaquinol (MK) is presented as bright green colored solid spheres and the phospholipids as yellow sticks.

Movie 2. The composition and structure of CIII dimer. Cartoon representation of the complex III. The menaquinone/menaquinol (MK) is presented as bright green colored solid spheres and the phospholipids as yellow sticks.

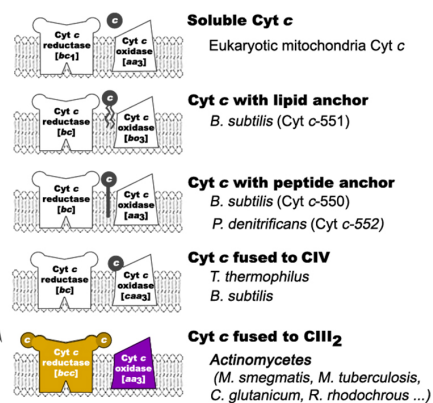
Movie 3. The composition and structure of CIV. Cartoon representation of the complex IV. The phospholipids are shown as yellow sticks.

A

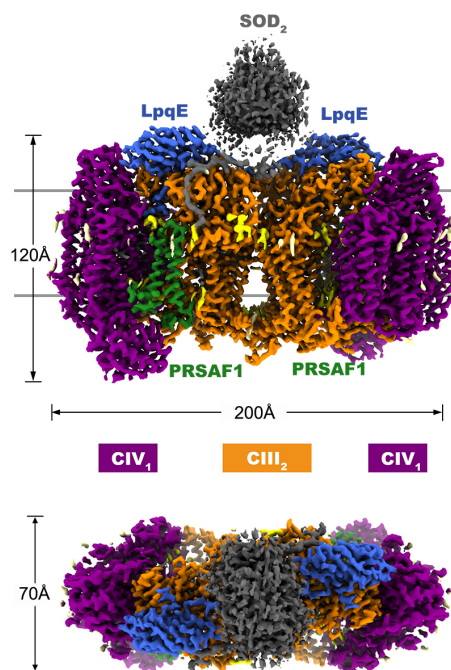
Respiration and oxidative phosphorylation in *Actinomyces*



Cytochrome *c* pathway variants



B



C

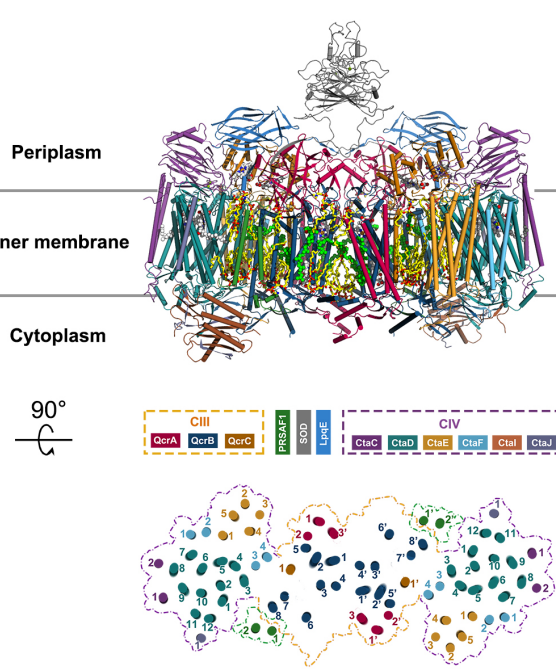


Figure 1

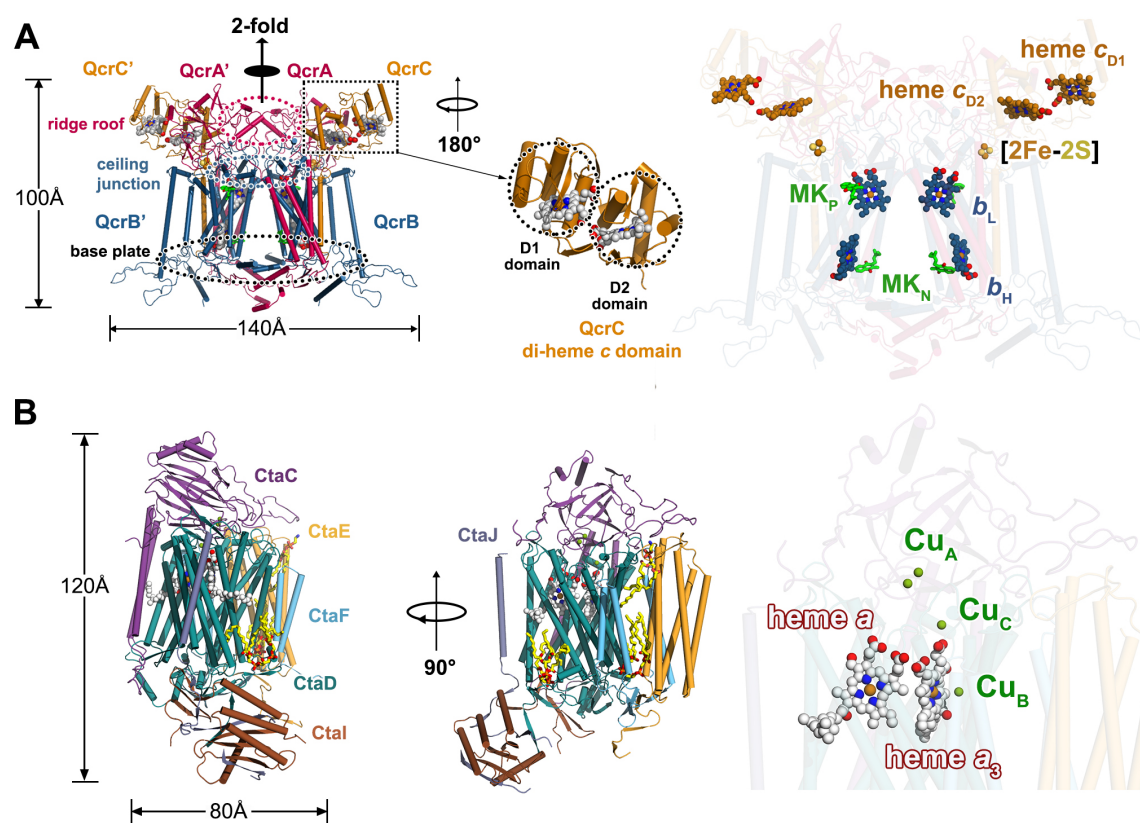
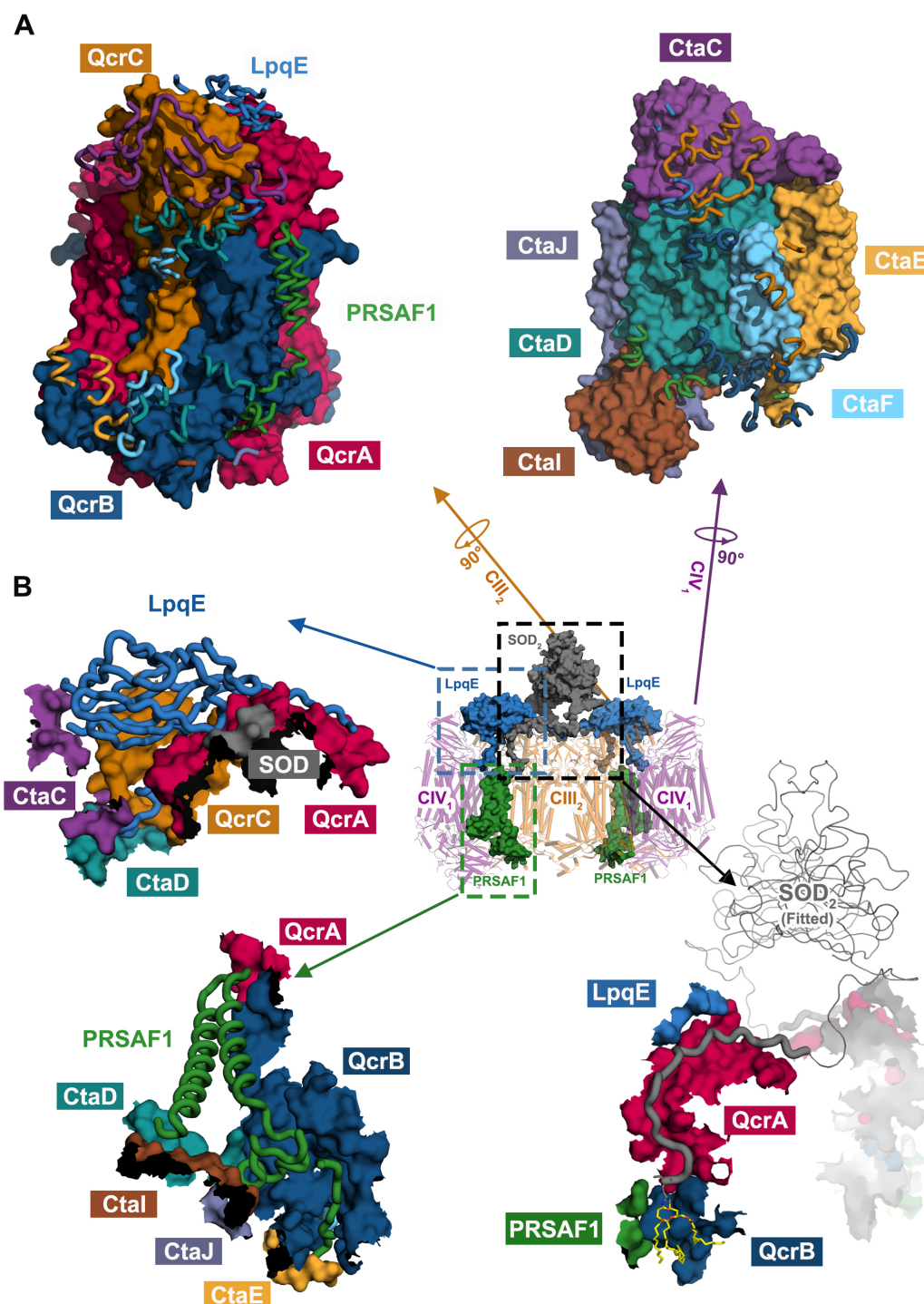


Figure 2



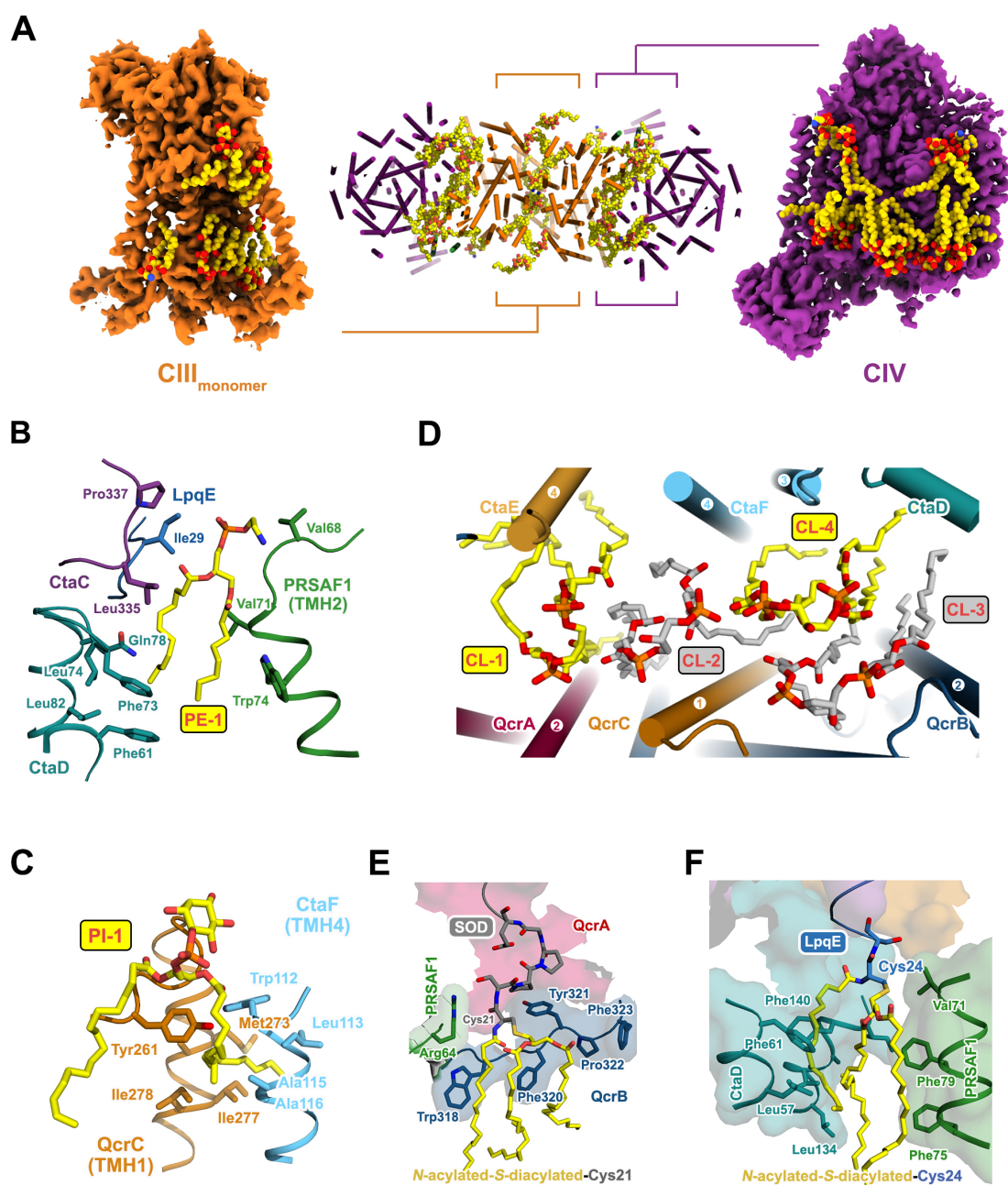


Figure 4

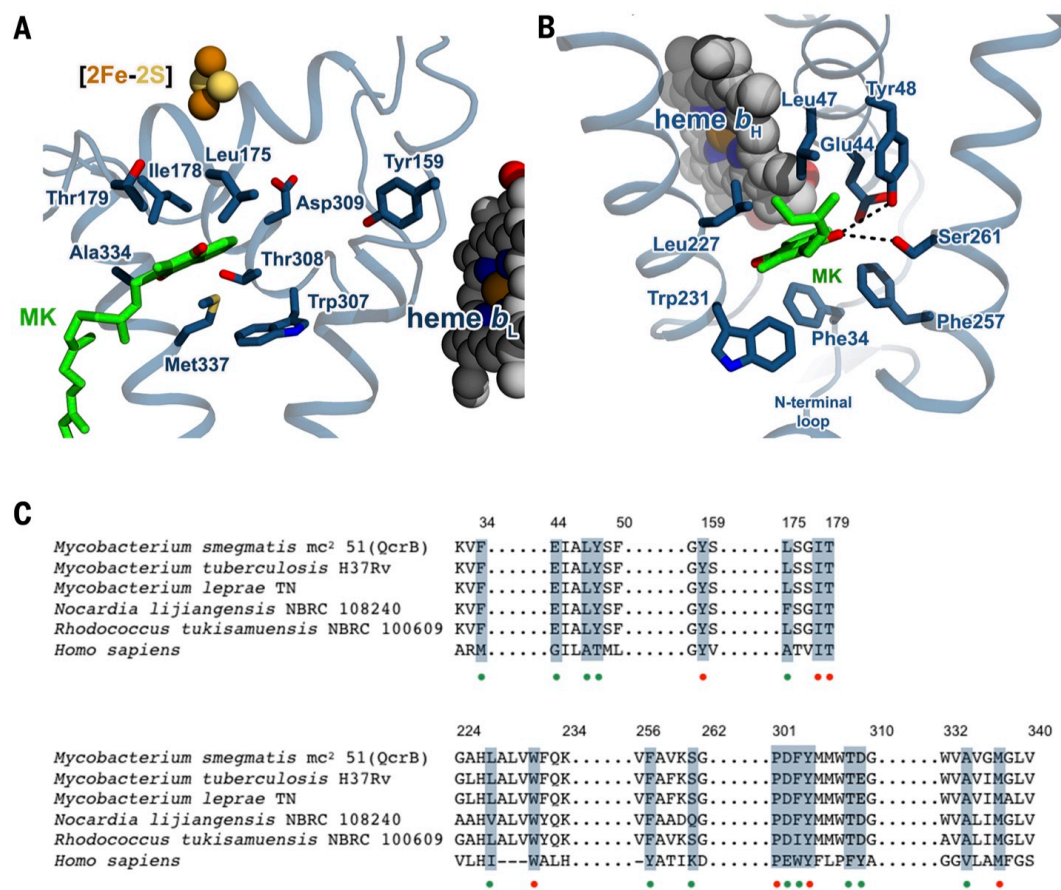


Figure 5

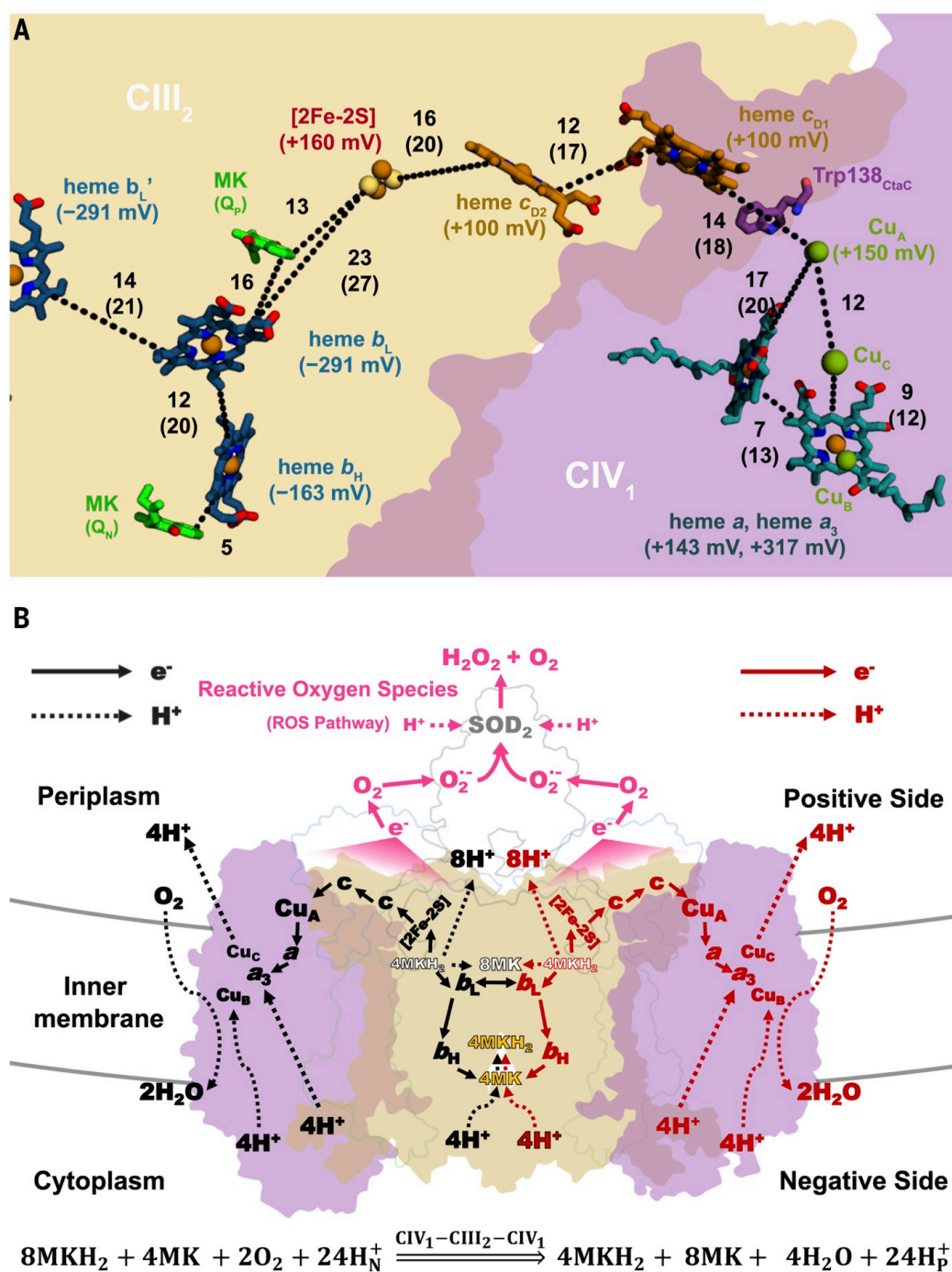


Figure 6